# From Detection to Rupture: A Serial Computational Fluid Dynamics Case Study of a Rapidly-Expanding, Patient-Specific, Ruptured Abdominal Aortic Aneurysm

**Barry J. Doyle,[1,2] Timothy M. McGloughlin[3] and Peter R. Hoskins[2,4]**

[1] Intelligent Systems for Medicine Laboratory, School of Mechanical and Chemical Engineering, The University of Western Australia, Australia.

[2] Centre for Cardiovascular Science, The University of Edinburgh, UK.

[3] Centre for Applied Biomedical Engineering Research (CABER), Department of Mechanical, Aeronautical and Biomedical Engineering, and Materials and Surface Science Institute, University of Limerick, Ireland.

[4] Department of Mechanical, Aeronautical and Biomedical Engineering, University of Limerick, Ireland.

**Abstract.** Computational hemodynamic studies of abdominal aortic aneurysm (AAA) can help elucidate the mechanisms responsible for growth and development. The aim of this work is to determine if AAAs expand and develop intraluminal thrombus (ILT) in regions of low wall shear stress (WSS) predicted with computational fluid dynamics (CFD). Computed tomography (CT) data of an AAA was acquired at four time-points over 2.5 years, from the time of detection to immediately prior to rupture. We used 3D unsteady, laminar, CFD models to investigate the hemodynamics at each time-point. Our three dimensional reconstructions showed that the primary region of expansion was in the proximal lobe, which not only coincided with the main region of low TAWSS in our CFD simulations, but also with the development of ILT in vivo. Interestingly, this region was also the rupture location. This is the first serial computational study of an AAA and the work has shown the potential of CFD to model the changing hemodynamics and the relation with ILT development and AAA growth.

# 1   Introduction

Abdominal aortic aneurysm (AAA) is typically an asymptomatic disease that is a significant cause of death in the developed world. These aneurysms are focal regions of dilation that form in the distal region of the aorta and can progress to the point of rupture. Maximum diameter is the traditional criterion for rupture-threat, with cases > 55 mm deemed at high risk. When the risk of rupture outweighs the risks associated with surgery, repair is often performed. However, several alternative risk factors have been proposed that can improve the current selection criteria for AAA repair [1-4].

AAAs have complex three dimensional (3D) geometries with many regions of inflection [5] and curvature [6] that influence the biomechanics of the disease [7, 8]. Developments in non-invasive imaging, software technologies and numerical techniques have enabled patient-specific modeling to better inform clinicians and allow for more accurate surgical planning [9]. Computational fluid dynamics (CFD) has been used to investigate AAA hemodynamics under rest and exercise [10], in different types of AAA [11], the design and evaluation of new AAA devices [12] and also to simulate aneurysm growth and development [13].

Abnormal hemodynamics within the abdominal aorta, such as high, low or oscillatory wall shear stress (WSS), have been correlated with atherosclerosis through experimental studies [14], numerical investigations [15] and also autopsy records [16]. It is believed that low WSS promotes vessel expansion and this has been successfully associated in cerebral aneurysms using CFD and medical imaging [17]; albeit, using only two clinical time-points. It remains to be demonstrated that AAAs expand in regions of low WSS.

Another important element of AAAs is the intraluminal thrombus (ILT). ILT is found in over 70% of clinically-relevant AAAs, yet the role of thrombus is still uncertain. Whether it provides a shielding effect by reducing the tensile stress acting on the wall [18], or if the ILT-induced hypoxia [19] outweighs the potential shielding benefits thus rendering the wall behind thick ILT vulnerable to rupture, is still under debate. Nevertheless, the hemodynamics associated with ILT formation and progression needs to be fully elucidated. Recently, Biasetti et al. [20] described ILT formation using abnormal hemodynamics as the key parameter responsible for platelet activation and thrombus development. Basciano et al. [21] also used CFD to model ILT development, where particle residence time (PRT) was used to depict platelet adhesion and aggregation, thus leading to ILT onset and advancement. Hardman et al. [22] also reported the PRT in AAAs, this time

using a novel WSS-limiter to model the attachment of monocytes to the luminal wall. It has been shown that ILT is likely to develop in areas of stagnated flow and low WSS, but not confirmed using follow-up medical imaging.

Therefore, the aim of this work was to examine if regions of low WSS spatially correlate with areas of expansion and thrombus development using serial medical imaging and CFD modeling.


## 2   Methods

We selected one male AAA patient from our database. This retrospective study was approved by the local ethics committee and was performed with the written, informed consent of the participant, complying with the Declaration of Helsinki. The case was an emergency open-repair for known AAA rupture, with the location of rupture recorded during the surgery.

The patient was imaged using contrast-enhanced computed tomography (CT) on a Siemens Sensation 64 (Siemens, Germany). Image parameters were: 3 mm slice thickness; 3 mm slice increment; and a pixel size of 0.74 mm. CT was performed at four time-points over the course of routine AAA management, with the final CT scan taken immediately prior to emergency surgical repair.

Each CT dataset was reconstructed into 3D using our previously described techniques [23, 24] in Mimics v15 (Materialise, Belgium). We reconstructed the lumen from immediately below the renal arteries to a point distal to the iliac bifurcation. 3D models were then exported to 3-matic v6.0 (Materialise, Belgium) for further pre-processing. We also reconstructed the ILT into 3D for analysis. All diameter measurements are the best-fit diameters determined from the 3D models and centerlines.

We then smoothed the 3D lumen surface geometry using 3-matic v6.0 in order to remove surface artifacts that remain after reconstruction, while maintaining the key features of the geometry. The resulting lumen geometries are shown in Fig. 1. Each model was modified to include entrance lengths and outlets, ensuring that faces remained normal to the centerline flow (see Fig. 2). The inlet face was extended by 59 mm, as calculated from the work of Wood [25] for unsteady flow, whereas the outlets were extended by 11 times the outlet diameter [22, 26, 27]. This outlet length was previously shown to have negligible influence on the upstream hemodynamics of experimental AAA models [26]. All relevant patient and

geometric details are shown in Table 1. We measured the volume using Mimics v15 and the ILT thickness using 3-matic v6.0.
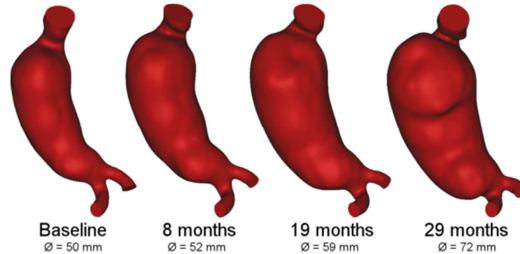


Fig. 1. 3D reconstructions of the lumen geometries at each time-point. Maximum best-fit lumen diameter is also shown below each model. All reconstructions begin at the renal arteries and end distal to the bifurcation, with proximal and distal faces cut orthogonal to the centerline. Models are shown from the posterior view

Each model was discretized into unstructured tetrahedral elements together with a boundary layer of prism elements using ICEM CFD 13.0 (ANSYS Inc.), whereby the total boundary layer thickness was equal to 30% of the outlet radii [28]. We used Fluent 13.0 (ANSYS Inc.) to solve the Navier-Stokes equations. To ensure our simulations were adequately resolved, *'Time1'* was modeled using three mesh densities, where each mesh size approximately doubled in number. We investigated mesh independence using a laminar, steady flow with an inlet Reynolds number of 1400 [21] and as the downstream pressure is unknown, we assigned an equally divided outflow boundary condition to the outlet face of the iliac artery extension lengths [27, 29]. We used the Grid Convergence Index (GCI) [30] to determine the necessary level of model refinement and the impact of mesh density, time step and cycle number on the results. The GCI is considered a very robust method of reporting error associated with discretization and its use is encouraged within the fluids engineering community [31]. For this purpose we averaged the WSS around four circumferential sections in the key regions of the model and then used these sections as a comparison tool to determine GCI. The optimum maximum tetrahedral and prism element edge length was found to be 1.5 mm and the boundary layer mesh consisted of six layers of prism elements. The boundary mesh element thickness also became progressively smaller as it approached the lumen wall. Element thickness adjacent to the lumen wall was in the range of 6 - 100 µm, thus, the boundary layer was sufficient to resolve the velocity gradient at the wall and accurately estimate WSS [32]. This specific mesh size returned a percentage error of < 2% and a GCI of 2.5%. As a result our final meshes had on average ± standard deviation (range), 1.29 ± 0.42 (0.94 - 1.98) million elements, depending on the geometry of the model. A representative numerical model is shown

in Fig. 2. For all simulations we assumed blood to be an incompressible, homogenous, Newtonian fluid, with a density of 1050 Kgm$^{-3}$ and viscosity of 0.0035 Pa s. The models were assumed to have rigid walls employing the no-slip condition and the blood flow was assumed to be laminar. These are common model assumptions when simulating the hemodynamics in large arteries [12, 21, 22, 27, 29, 32-34].

To simulate the pulsatile blood flow, we developed a custom-written user-defined function inlet boundary condition in MATLAB (The Mathworks Inc.). This mass flow inlet represented an average waveform of 21 AAA patients previously examined using Doppler ultrasound by Fraser et al. [35]. We applied a flat plug inlet profile to the face of the entrance length as the effects of more realistic inlet profiles are secondary to the influences of the geometry [33]. As with our steady simulations, the outlet pressure was unknown and so an equally-divided outflow condition was prescribed to the outlet faces. We used the Pressure Implicit with Splitting Operators (PISO) pressure-velocity coupling algorithm within Fluent 13.0, together with 250 time-steps per cardiac cycle. In a sub-study, we found that by doubling and quadrupling the number of time-steps resulted in a GCI of 0.8% and that our results were periodic from the third cycle onwards. As such, each simulation was run for three full cardiac cycles, with data only interpreted from the third cycle. Convergence criteria were set to 1 x 10$^{-4}$ for mass and 1 x 10$^{-3}$ for momentum for all simulations.

We determined time-averaged WSS (TAWSS) by collecting WSS data at regular intervals of the cardiac cycle and averaging over the total time (t = 0.92 s). This post-processing was performed using a custom-written MATLAB script which generated 3D contour plots of TAWSS. TAWSS data and maximum best-fit diameter was then plotted against the normalized longitudinal distance for each clinical time-point. We also spatially compared TAWSS with ILT development. We tested for possible relationships between TAWSS and diameter using Spearman's non-parametric correlation tests with a p-value < 0.05 deemed significant.

## 3    Results

The quantitative changes in geometry, volume and maximum ILT thickness are presented in Table 2. The ILT increased in volume at a rate of 9 cm$^3$/year (range = 7 - 29 cm$^3$) over 29 months. The physical evolution of the ILT is shown in Fig. 3. Local maximum ILT thickness peaked at 19 months with the thrombus then becoming thinner yet larger in volume. There was no appreciable change in the lumen centerline tortuosity of each model over time.

With the exception of *Time2*, the proximal lobe of each model experienced low TAWSS throughout the growth period (Fig. 3). ILT developed in a region of low TAWSS in the proximal lobe. TAWSS was inversely related to the maximum best-fit diameter of the lumen. This relationship was significant at certain time-points during the growth period and approaching significance at others (*Time1*, $p = 0.073$; *Time2*, $p = 0.007$; *Time3*, $p = 0.056$; *Time4*, $p = 0.016$).

Table 1: Patient details and best-fit diameters at each imaging time-point.

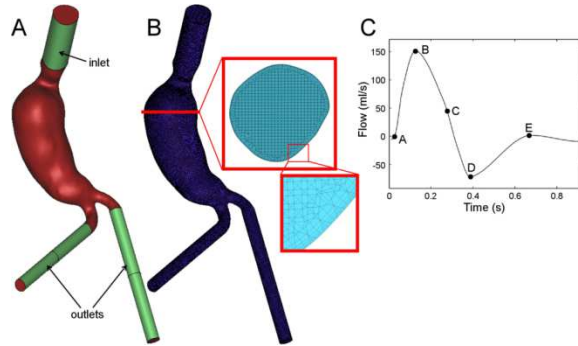| Study ID | Time (months) | Age (years) | Maximum Lumen Diameter (mm) | Inlet Diameter (mm) | Right Iliac Diameter (mm) | Left Iliac Diameter (mm) |
|---|---|---|---|---|---|---|
| Time1 | Baseline | 75 | 50.1 | 22.2 | 10.9 | 10.9 |
| Time2 | 8 | 76 | 51.9 | 21.0 | 9.3 | 10.3 |
| Time3 | 19 | 77 | 58.9 | 22.1 | 9.8 | 10.4 |
| Time4 | 29 | 78 | 71.7 | 24.0 | 11.7 | 11.4 |



Fig. 2. (A) Example 3D model *(Time1)* with inlet and outlet extensions shown and (B) meshed model with cross-section illustrating typical mesh density and the progressive six-layer boundary mesh. (C) Inlet flow waveform determined from 21 AAA patients [35]. The relevant time-points within the cardiac cycle are also indicated (a-e). The total length of this cardiac cycle is 0.92 s.

The clinical location of rupture was noted as "inferior to the left renal artery" at the time of emergency open-repair and was illustrated using a simple intra-operative sketch. Fig. 4 shows the TAWSS contours compared to the location of

rupture. Fig. 5 shows the pathlines of particles seeded from the inlet at the time of peak systolic flow at each of the four time-points.

Table 2: ILT and lumen volumes, maximum ILT thickness, tortuosity and best-fit diameter for each model examined. Percentage changes are from that of the previous time-point.

| Study ID | Time (months) | ILT Volume (cm$^3$) | % Change in ILT Volume | ILT Thickness (mm) | % Change in ILT Thickness | Lumen Volume (cm$^3$) | % Change in Lumen Volume |
|---|---|---|---|---|---|---|---|
| Time1 | Baseline | 7.4 | - | 7 | - | 140.6 | - |
| Time2 | 8 | 9.8 | 32 | 10 | 43 | 167.9 | 19 |
| Time3 | 19 | 19.7 | 101 | 15 | 50 | 227.7 | 36 |
| Time4 | 29 | 28.6 | 45 | 14 | -7 | 344.6 | 51 |

## 4 Discussion

We have computationally investigated a rapidly-expanding, patient-specific ruptured AAA from the time of detection to rupture, over 2.5 years. Our results show that, in this particular case, lumen expansion and ILT development spatially coincide with areas of low TAWSS.

The proximal lobe of the lumen experienced low TAWSS throughout the rapid-expansion (9 mm/year) period prior to rupture. This proximal lobe also later became the rupture site. According to the literature, the majority of AAAs rupture into the retroperitoneum [37] and posterior-inferior regions [38]. The rupture location in this instance is not typical and is within the 18% of those that rupture superior to the maximum dilation region [38] and within the 10% that rupture inferior to the left renal artery [37]. Additionally, according to da Silva et al. [38], ILT is found at the site of rupture in 80% of cases, with the remaining 20% experiencing rupture at areas without thrombus or at the transition of an area with thrombus and without it. Indeed, by comparing the intra-operative sketch to the 3D reconstruction at 29 months (see Fig. 4) it would appear that rupture occurred in or around the region of ILT here.

It is known that low WSS facilitates arterial remodeling through apoptosis [39] and proliferation, in particular when the WSS < 0.4 Pa [36]. Below this level, ath-

erogenic phenotypes are stimulated, thus enabling the breakdown of the endothelium. Monocytes adhere to the endothelium in regions where WSS < 0.36 Pa [40-42] and as the WSS tends to zero, the adhesion efficiency increases exponentially [42], further contributing to the expansion process. From our simulations it would appear that this particular AAA ruptured at a region experiencing TAWSS below this critical threshold of 0.4 Pa (Fig. 4). Interestingly, the pathlines shown in Fig. 5 at peak systolic flow for each clinical time-point reveal how the hemodynamics may have contributed to rupture through recirculation in the proximal region over time. Thus, the development of low velocity near-wall flow and reduced TAWSS may each have contributed to expansion and ILT development. However, this work needs to be extended to other AAA cases to confirm if this finding is unique to this particular case.

It has been previously described how ILT may develop in the distal region of an AAA as particles tend to attach to the wall downstream in the sac [11, 20, 21, 43]. However, in this AAA, ILT only developed in the proximal region where it is likely that platelets were trapped in the recirculating low TAWSS region and deposited to the wall. We can attempt to explain the lack of distal ILT observed in this case by the following hypothesis. It is known that the endothelial layer is a key factor in thrombosis and contributes to the development of ILT in AAA. A healthy aorta exhibits an intact endothelial layer that controls hemostasis and thrombosis, whereas, in AAA disease this layer is often deteriorated and the luminal surface becomes thrombogenic. It is plausible that this aneurysm evolved quicker than the degeneration rate of the endothelial layer and therefore, the WSS along the length of the lumen still activated endothelial cells and provided anti-thrombogenic properties. It was only in the proximal region of recirculation and low WSS that the endothelial layer was degraded and ILT subsequently developed. However, further testing in conjunction with histology is required to prove this theory.

Particle residence time (PRT) is a useful parameter to indicate monocyte deposition and attachment [21, 22, 43, 44] and may be particularly beneficial in conjunction with longitudinal medical imaging. In recent work by Biasetti et al. [20], a $\lambda_2$-method [45] and vortical structure (VS) approach was described as a potential mechanism for modeling ILT formation. In order to fully elucidate the hemodynamics involved in AAA and ILT evolution, it may be necessary in to combine PRT and VS models, together with advanced approaches to determine patient-specific inlet and downstream boundary conditions, and verify results using medical imaging and histology.

In addition, there are other limitations to our study to should be addressed in future investigations. The use of a deformable wall and the incorporation of fluid-

structure interaction (FSI) may further enhance our results [46]. Multi-scale approaches have been used to model outlet boundary conditions [47] and also represent a likely improvement over the outlet boundary condition employed here. Finally, our results should be interpreted with caution as longitudinal imaging was only available for one AAA case. This type of study needs to be expanded to a large cohort of patients with stable, symptomatic and ruptured AAAs, from all diameter and growth rate ranges, to determine if the findings presented here are statistically significant and have clinical relevance.
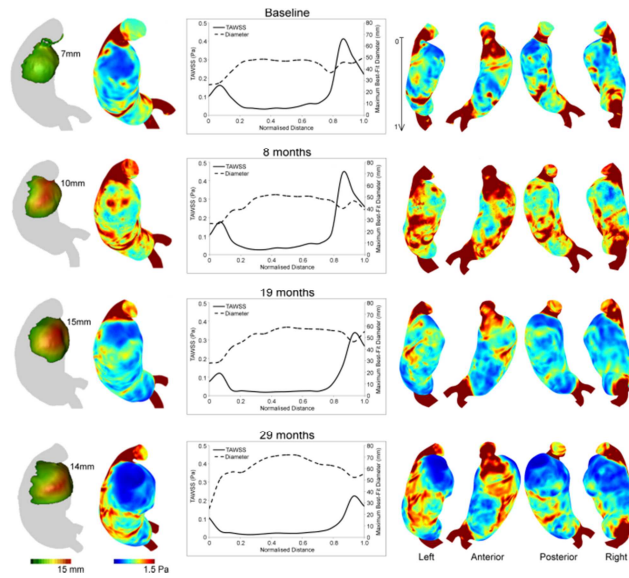


Fig. 3. ILT thickness *(far left)*, TAWSS contours and TAWSS-diameter plots at each time-point. The ILT thickness scale refers to all models in the far left column. The TAWSS scale refers to all TAWSS contour plots. TAWSS was scaled to a maximum of 1.5 Pa [36]. The normalized distance begins (0) at the proximal neck and ends (1) distal to the iliac bifurcation, as shown in the top row of TAWSS plots.

## 5 Conclusions

In this single, longitudinal case study, regions of low TAWSS correlated with areas of lumen expansion and ILT development. Rupture occurred in the proximal, low TAWSS region of the AAA where the flow was recirculating. This is the first report in the literature where CFD was performed using serial medical imaging and could help future research to fully elucidate the role of low WSS in AAA expansion and thrombus development.
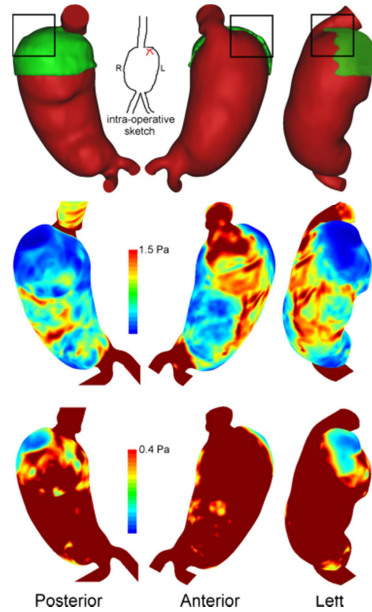
Posterior    Anterior    Left

Fig. 4. Comparison of the clinical rupture location observed during emergency open-repair *(intra-operative sketch)* indicated on the 3D reconstruction *(black box)* and TAWSS contours at time of rupture. TAWSS is shown scaled to 1.5 Pa [36] and 0.4 Pa [39].

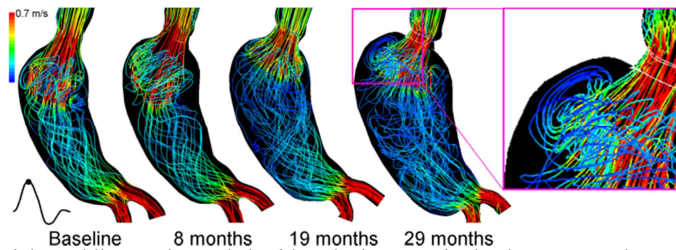

Baseline    8 months    19 months    29 months

Fig. 5. Particle pathlines color-coded with velocity magnitude shown at peak systolic flow at each clinical time-point. Models are shown from the posterior view. Inset shows pathlines in the rupture region.

# References

1. Doyle BJ, Callanan A, Burke PE et al (2009) Vessel asymmetry as an additional diagnostic tool in the assessment of abdominal aortic aneurysms. J Vasc Surg 49:443-454.
2. Vande Geest JP, Di Martino ES, Bohra A et al (2006) A biomechanics-based rupture potential index for abdominal aortic aneurysm risk assessment: demonstrative application. Ann NY Acad Sci 1085:11-21.
3. Kleinstreuer C, Li Z (2006) Analysis and computer program for rupture-risk prediction of abdominal aortic aneurysms. Biomed Eng Online 5:19.

4. Gasser TC, Auer M, Labruto F et al (2010) Biomechanical rupture risk assessment of abdominal aortic aneurysms: model complexity versus predictability of finite element simulations. Eur J Vasc Endovasc Surg 40:176-85.

5. Doyle BJ, Killion J, Callanan A (2012) Use of the photoelastic method and finite element analysis in the assessment of wall strain in abdominal aortic aneurysm models. J Biomech 45:1759-1768.

6. Sacks MS, Vorp DA, Raghavan M et al (1999) In vivo three-dimensional surface geometry of abdominal aortic aneurysms. Ann Biomed Eng 27:469-479.

7. Vorp DA, Vande Geest JP (2005) Biomechanical determinants of abdominal aortic aneurysm rupture. Arterioscl Thromb Vasc Biol 25:1558-1566.

8. McGloughlin TM, Doyle BJ (2010) New approaches to abdominal aortic aneurysm rupture risk assessment: engineering insights with clinical gain. Arterioscl Thromb Vasc Biol 30:1687-1694.

9. Doyle BJ, Grace PA, Kavanagh EG et al (2009) Improved assessment and treatment of abdominal aortic aneurysms: the use of 3D reconstructions as a surgical guidance tool in endovascular repair. Ir J Med Sci 178:321-328.

10. Les AS, Shadden SC, Figueroa CA et al (2010) Quantification of hemodynamics in abdominal aortic aneurysms during rest and exercise using magnetic resonance imaging and computational fluid dynamics. Ann Biomed Eng 38:1288-1313.

11. Biasetti J, Gasser T, Auer M et al (2010) Hemodynamics of the normal aorta compared to fusiform and saccular abdominal aortic aneurysms with emphasis on a potential thrombus formation mechanism. Ann Biomed Eng 38:380-390.

12. Molony DS, Callanan A, Morris LG et al (2008) Geometrical enhancements for abdominal aortic stent-grafts. J Endovasc Ther 15:518-529.

13. Sheidaei A, Hunley SC, Zeinali-Davarani S et al (2011) Simulation of abdominal aortic aneurysm growth with updating hemodynamic loads using a realistic geometry. Med Eng Phys 33:80-88.

14. Moore J, Maier S, Ku D et al (1994) Hemodynamics in the abdominal aorta: a comparison of in vitro and in vivo measurements. J App Physiol 76:1520-1527.

15. Tang BT, Cheng CP, Draney MT et al (2006) Abdominal aortic hemodynamics in young healthy adults at rest and during lower limb exercise: quantification using image-based computer modeling. Am J Physiol Heart Circ Physiol 291:668-676.

16. Cornhill JF, Herderick EE, Stary HC (1990) Topography of human aortic sudanophilic lesions. Monogr Atheroscler 15:13-19.

17. Boussel L, Rayz V, McCulloch C et al (2008) Aneurysm growth occurs at region of low wall shear stress: patient-specific correlation of hemodynamics and growth in a longitudinal study. Stroke 39:2997-3002.

18. Wang D, Makaroun M, Webster M et al (2002) Effect of intraluminal thrombus on wall stress in patient-specific models of abdominal aortic aneurysm. J Vasc Surg 36:598-604.

19. Vorp D, Lee P, Wang D et al (2001) Association of intraluminal thrombus in abdominal aortic aneurysm with local hypoxia and wall weakening. J Vasc Surg 34:291-299.

20. Biasetti J, Hussain F, Gasser TC (2011) Blood flow and coherent vortices in the normal and aneurysmatic aortas: a fluid dynamical approach to intra-luminal thrombus formation. J R Soc Interface 8:1449-1461.

21. Basciano C, Kleinstreuer C, Hyun S et al (2011) A relation between near-wall particle-hemodynamics and onset of thrombus formation in abdominal aortic aneurysms. Ann Biomed Eng 39:2010-2026.

22. Hardman D, Doyle BJ, Semple SIK et al (2013) On the prediction of monocute depostition in abdominal aortic aneurysms. J Eng Med, in press.

23. Doyle B, Callanan A, McGloughlin TM (2007) A comparison of modeling techniques for computing wall stress in abdominal aortic aneurysms. Biomed Eng Online 6:38.

24. Doyle B, Morris L, Callanan A et al (2008) 3D reconstruction and manufacture of real abdominal aortic aneurysms: from ct scan to silicone model. J Biomech Eng 130:034501.

12

25. Wood NB (1999) Aspects of fluid dynamics applied to the larger arteries. J Theor Biol 199:137-61.
26. Egelhoff CJ, Budwig RS, Elger DF et al (1999) Model studies of the flow in abdominal aortic aneurysms during resting and exercise conditions. J Biomech 32:1319-1329.
27. Hardman D, Semple SI, Richards JM et al (2013) Comparison of patient-specific inlet boundary conditions in the numerical modeling of blood flow in abdominal aortic aneurysm disease. Int J Num Meth Biomed Eng 29:165-178.
28. Suh GY, Les AS, Tenforde AS et al (2011) quantification of particle residence time in abdominal aortic aneurysms using magnetic resonance imaging and computational fluid dynamics. Ann Biomed Eng 39:864-883.
29. ANSYS (2010) ANSYS Fluent User's Guide.
30. Roache PJ (1994) Perspective: a method for uniform reporting of grid refinement studies. J Fluids Eng 116:405-413.
31. Celik IB, Ghia U, Roache PJ et al (2008) Procedure for estimation and reporting of uncertainty due to discretization in cfd applications. J Fluids Eng 130:078001.
32. Sazonov I, Nithiarasu P (2012) Semi-automatic surface and volume mesh generation for subject-specific biomedical geometries. Int J Num Meth Biomed Eng 28:133-157.
33. Morris L, Delassus P, Grace P et al (2006) Effects of flat, parabolic and realistic steady flow inlet profiles on idealised and realistic stent graft fits through abdominal aortic aneurysms (AAA). Med Eng Phys 28:19-26.
34. Molony DS, Callanan A, Kavanagh EG et al (2009) Fluid-structure interaction of a patient-specific abdominal aortic aneurysm treated with an endovascular stent-graft. Biomed Eng Online 8:24.
35. Fraser KH, Meagher S, Blake J et al (2008) Characterization of an abdominal aortic velocity waveform in patients with abdominal aortic aneurysm. Ultrasound Med Biol 34:73-80.
36. Malek AM, Alper SL, Izumo S (1999) Hemodynamic shear stress and its role in atherosclerosis. JAMA 282:2035-2042.
37. Darling R, Messina C, Brewster D et al (1977) Autopsy study of unoperated abdominal aortic aneurysms. the case for early resection. Circ 56:161-164.
38. da Silva ES, Rodrigues AJ, Magalhes Castro De Tolosa E et al (2000) Morphology and diameter of infrarenal aortic aneurysms: a prospective autopsy study. Cardiovasc Surg 8:526-532.
39. Kaiser D, Freyberg MA, Friedl P (1997) Lack of hemodynamic forces triggers apoptosis in vascular endothelial cells. Biochem Biophys Res Commun 231:586-590.
40. Lawrence MB, Berg EL, Butcher EC et al (1995) Rolling of lymphocytes and neutrophils on peripheral node addressin and subsequent arrest on ICAM-1 in shear flow. Eur J Immunol 25:1025-1031.
41. Lawrence MB, McIntire LV, Eskin SG (1987) Effect of flow on polymorphonuclear leukocyte/endothelial cell adhesion. Blood 70:1284-1290.
42. Worthen GS, Smedly LA, Tonnesen MG et al (1987) Effects of shear stress on adhesive interaction between neutrophils and cultured endothelial cells. J Appl Physiol 63:2031-2041.
43. Hardman D, Easson WJ, Hoskins PR (2010) Computation of the distribution of monocyte deposition in abdominal aortic aneurysm disease. In: Dossel O, Schlegel WC (eds) World congress on medical physics and biomedical engineering. IFMBE Proc 25:1961-1964.
44. Rayz VL, Boussel L, Ge L et al (2010) Flow residence time and regions of intraluminal thrombus deposition in intracranial aneurysms. Ann Biomed Eng 38:3058-3069.
45. Jeong J, Hussain F (1995) on the identification of a vortex. J Fluid Mech 285:69-94.
46. Fraser KH, Li MX, Lee WT et al (2009) Fluid-structure interaction in axially symmetric models of abdominal aortic aneurysms. J Eng Med 223:195-209.
47. Vignon-Clementel I, Figueroa CA, Jansen K et al (2006) Outflow boundary conditions for three-dimensional finite element modeling of blood flow and pressure in arteries. Comp Meth Appl Mech Eng 195:3776-3796.